Journal of
Materials Chemistry A

Materials for energy and sustainability

Accepted Manuscript

This article can be cited before page numbers have been issued, to do this please use: H. Cui, H. Mi, C. Ji, F. Guo, Y. Chen, D. Wu, J. Qiu and H. Xie, *J. Mater. Chem. A*, 2021, DOI: 10.1039/D1TA06974H.

ROYAL SOCIETY OF CHEMISTRY

rsc.li/materials-a

View Article Online
DOI: 10.1039/D1TA06974H

ARTICLE

A durable MXene-based zinc ion hybrid supercapacitor with sulfated polysaccharide reinforced hydrogel/electrolyte

Received 00th January 20xx,
Accepted 00th January 20xx

DOI: 10.1039/x0xx00000x

Haonan Cui[a], Hongyu Mi[a,*], Chenchen Ji[a,c,*], Fengjiao Guo[a], Yanna Chen[a], Dandan Wu[a], Jieshan Qiu[b,*], Haijiao Xie[d]

Abstract: Zn-ion hybrid supercapacitors (ZHSCs) emerge as promising equipment for energy storage applications due to their eco-efficiency, abundant natural resource, and high safety. However, the development of ZHSCs remains at the initial stage and substantial efforts in electrode materials and hydrogel/electrolytes are still needed for further enhancing its charge storage ability. Herein, a crumpled nitrogen-doped MXene wrapped with nitrogen-doped amorphous carbon (denoted as NMXC) was synthesized through a template-guided route for modulating the surface chemistry and expanding the inter-lamellar spacing of MXene. Density functional theory (DFT) calculation reveals that N-doping effect enhances the electronic conductivity of MXene and the MXene heterostructure with N-doped carbon layer possesses an enlarged work function compared with pure MXene, which effectively prevents the electrochemical oxidation and enables stable operation at higher positive potential. Due to these reasons, NMXC exhibits a higher capacity and wider operating voltage window compared with pure MXene and better rate performance than melamine formaldehyde derived N-doped carbon (NC). Moreover, a dual crosslinked hybrid polymeric hydrogel/electrolyte (denoted as PAM-co-PAA/κ-CG/$ZnSO_4$) was also designed, which was obtained by forming inter-molecular hydrogen bonds between ionic κ-carrageenan (denoted as κ-CG) double helices chain and covalent poly(acrylic amide-acrylic acid) (denoted as PAM-co-PAA) main matrix. The test results show that the PAM-co-PAA/κ-CG/$ZnSO_4$ hydrogel/electrolyte possesses a higher ionic conductivity of 1.76 S m^{-1}, higher stretchability of 626.0%, and satisfactory compressibility. In addition, the quasi-solid-state ZHSC based on NMXC cathode and PAM-co-PAA/κ-CG/$ZnSO_4$ hydrogel/electrolyte demonstrates a low self-discharge rate of 1.75 mV h^{-1}, a high capacity with 96.4% capacity retention after 10000 cycles along with high energy/power densities of 54.9 W h kg^{-1}/3314.4 W kg^{-1}.

1. Introduction

The COVID-19 pandemic is argumentatively the greatest challenge facing humanity at present, which further emphasizes efforts at global scale need to be provided to build a harmonious society with sustainable development that respects the natural environment and inhabitants.[1] The same demands are also required for energy storage fields, and therefore, various clean power sources (*e.g.*, lithium ion batteries, supercapacitors, and fuel cells) are designed for decarbonizing transportation and directly reducing the greenhouse gas emissions, which are and will be responsible for decreasing the use of fossil fuels and mitigating climate changes.[1-9]

Among the burgeoning technologies, aqueous multivalent-metal-ion based (*e.g.*, Zn^{2+}, Mg^{2+}, Al^{3+}) rechargeable energy-storage equipment has aroused persistent research interests.[3, 10-13] In this regard, aqueous Zn ions hybrid supercapacitors (ZHSCs) deliver mixed characteristics of Zn-ion batteries and supercapacitors, holding great potential as power candidates due to the merits of inherent safety, eco-friendly, low price (about USD \$2 kg^{-1}), high theoretical capacity (820 mA h g^{-1}, 5855 mA h cm^{-3}), multi-electron transfer properties, low redox potential of metal Zn anode (-0.76 V vs. SHE), and fast charge transfer dynamics.[4-8,14,15] In addition, significant enhancements in boosting the energy densities have been made for ZHSCs during recent years via structural optimization of electrode materials and device designs.[16] These developments further enable this technology as ideal power sources for portable electronics.[17] Nevertheless, limited optional electrode

[a] School of Chemical Engineering and Technology, Xinjiang University, Urumqi 830046, People's Republic of China. E-mail: jichenchen2010@163.com; mmihongyu@163.com
[b] State Key Laboratory of Chemical Resource Engineering, College of Chemical Engineering, Beijing University of Chemical Technology, Beijing 100029, People's Republic of China. E-mail: qiujs@mail.buct.edu.cn
[c] State Key Laboratory of Fine Chemicals, Dalian University of Technology, Dalian 116024, People's Republic of China.
[d] Hangzhou Yanqu Information Technology Co., Ltd., Hangzhou 310003, People's Republic of China

† Footnotes relating to the title and/or authors should appear here.
Electronic Supplementary Information (ESI) available: [details of any supplementary information available should be included here]. See DOI: 10.1039/x0xx00000x

View Article Online
DOI: 10.1039/D1TA06974H

materials, unfavourable side reactions in aqueous electrolytes (*e.g.*, O_2 or H_2 evolution), irreversible by-products (*e.g.*, growth of Zn dendrites), leakage problem, and low battery efficiency severely impede the development of ZHSCs.[18-20]

To overcome the above limitations, two main strategies are commonly used. The first one consists of constructing of highly stable and effective electrode materials. It involves the broadening of the operational potential windows of the electrodes. Among the optional materials, recent findings suggest that two-dimensional (2D) MXene materials (*e.g.*, $Ti_3C_2T_x$, also known as transition metal carbide) with quantum confinement in one direction, excellent metallic electrical conductivity (up to 10000 S cm^{-1}), and hydrophilic surface property might provide promising perspectives for energy storage and conversion.[21,22] For instances, Nuno Bimbo et al. designed a ZHSC based on pillared MXene, which exhibits favourable capacities of 86 mA h g^{-1} at 20 mA g^{-1} and 27 mA h g^{-1} at 1000 mA g^{-1}, and maintained 96% of the initial capacity after 1000 charge/discharge cycles.[23] Zhi et al. reported a rechargeable Zn ion capacitor with the pure MXene as electrode material, which delivers a specific capacitance of 132 F g^{-1} at 0.5 A g^{-1} with 82.5% capacity retention after 1000 cycles.[24] However, MXene layers are highly prone to horizontal stacking, making them hard to provide sufficient tunnels for the electrolyte ion transfer and compromising the true ability for charge storage.[6, 25,26] In addition, pure MXene materials (*e.g.*, $Ti_3C_2T_x$) commonly display narrow potential windows as cathode for energy storages due to they are highly susceptible to be oxidized at anodic oxidation potential.[21, 25] In this context, employing nano-engineering techniques to boost the stability and energy storage capacities via heteroatomic doping and surface modification by intimately incorporation with second stable phase are critically desired.[21]

The second strategy is to introduce the relative stable ion-conductive polymer hydrogel/electrolytes.[18] This process replaces the liquid–solid interface with the solid–solid interface between electrolytes and electrodes, which effectively reduces the side reactions in aqueous electrolyte, enhances the charge storage stability, and restrains the growth of zinc dendrites.[27] In addition, polymer hydrogel/electrolytes also have the intrinsical characteristics of water-retaining capability to address liquid leakage problem.[20] However, the widely used hydrogel/electrolytes suffer from low ionic conductivity or unsatisfactory mechanical strength.[28] Hence, continuing effort is needed such as the structure reinforcement of the polymeric matrix via additional modification to develop more available and optional polymeric hydrogel/electrolytes for meeting the above requirements. In this regard, sulfated polysaccharides (*e.g.*, κ-carrageenan, one type of hydrophilic linear sulfated galactans) as one kind of natural gel material exist widely in living organisms, which may promote the cell proliferation & differentiation, tissue formation, and intercellular interactions.[29] These special functions of sulfated polysaccharides are highly depended on the special main body structures and sulfation functional groups, which enable fine-tune of structural properties.[29] Given its special structure and function, incorporating of ionic crosslinked sulfated polysaccharides into double network hydrogels with other covalently crosslinked main polymeric matrix would integrate the disparate physicochemical nature of individual network to further realize the augmented mechanical strength, enhanced water uptake capacity, and high ionic conductivity.

Herein, a crumpled nitrogen-doped MXene-based heterostructure wrapped with nitrogen-doped amorphous carbon (denoted as NMXC) was synthesized through a template-guided route. Experimental results demonstrate that the as-formed carbon layer could prevent the oxidation of MXene under higher potential while the poriferous framework is very likely to offer large specific surface area and sufficient space for electrolyte ions transfer. More importantly, density functional theory (DFT) calculation shows that the N dopants are energetically favourable for promoting the conductivity of MXene matrix and the heterostructure with nitrogen-doped carbon layer enhances the electrochemical stability at anodic potential due to the increscent work function (WF). Due to these reasons, NMXC can stably and efficiently store charges as cathode and exhibits a high specific capacity, boosted rate performance, and a long-term stability with 87.1% capacity retention after 9000 cycles under a wider voltage window. Moreover, a dual crosslinked hybrid polymeric hydrogel (denoted as PAM-co-PAA/κ-CG) was designed in this work, which was obtained by forming inter-molecular hydrogen bonds between the ionic κ-carrageenan (denoted as κ-CG) chain with the covalent poly(acrylic amide-acrylic acid) (denoted as PAM-co-PAA) copolymer main matrix. After adsorbing sufficient $ZnSO_4$ electrolyte, the soft conductive polymeric hydrogel/electrolyte (denoted as PAM-co-PAA/κ-CG/$ZnSO_4$) was obtained for ZHSC. The test results show that the hydrophilic PAM-co-PAA networks can adsorb sufficient electrolyte while the κ-CG reinforces mechanical properties. Due to these reasons, the PAM-co-PAA/κ-CG/$ZnSO_4$ hydrogel/electrolyte possesses a higher ionic conductivity of 1.76 S m^{-1}, higher stretchability of 626.0%, and

View Article Online
DOI: 10.1039/D1TA06974H

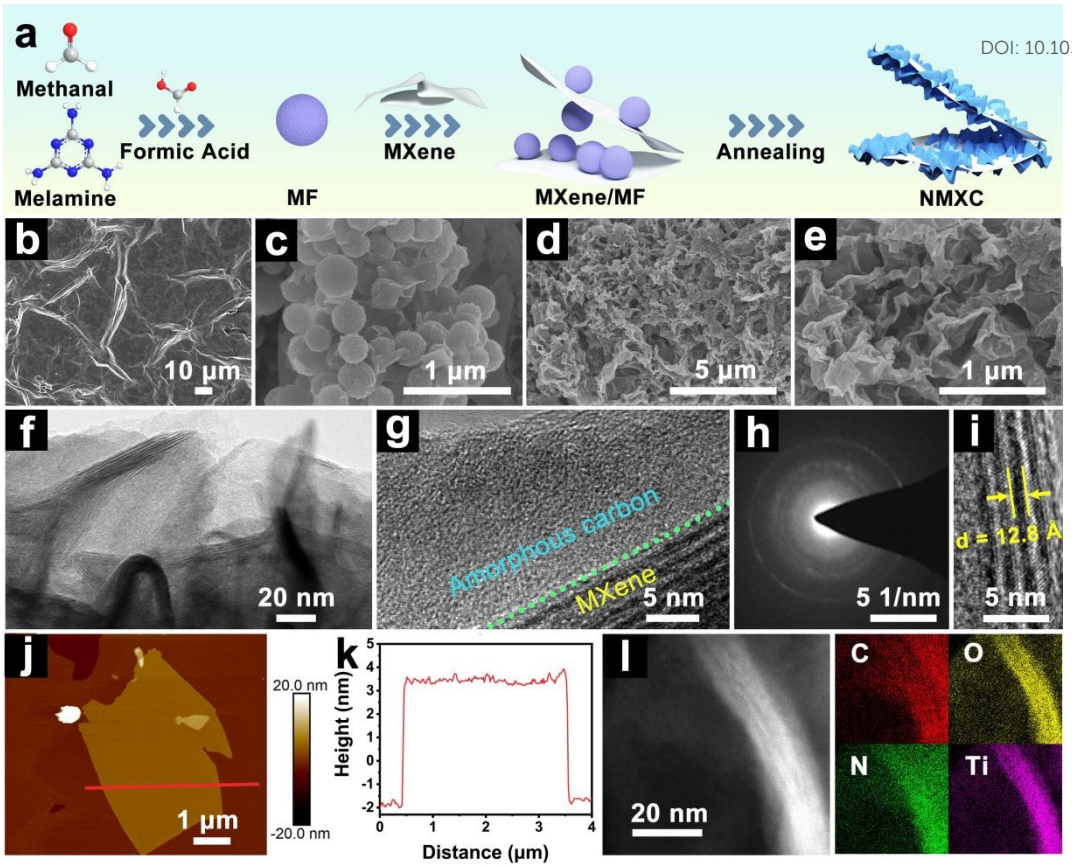

Fig. 1 Schematic illustration and structure characterization. (a) Schematic for the preparation of NMXC. SEM images of (b) MXene, (c) MXene/MF, and (d, e) crumpled NMXC with different magnification. (f) TEM image of NMXC. (g) HRTEM image shows the amorphous carbon layer of NMXC. (h) SAED pattern of NMXC. (i) HRTEM image shows the interlayer distances between two neighbouring MXene sheets. (j) AFM image and (k) thickness profile of NMXC. (l) HRTEM image and the corresponding elemental mapping images of NMXC.

desirable compressibility. In addition, the quasi-solid-state ZHSC based on NMXC cathode and PAM-co-PAA/κ-CG/$ZnSO_4$ hydrogel/electrolyte demonstrates a high capacity with 96.4% capacity retention after 10000 cycles along with high energy/power densities of 54.9 W h kg^{-1}/3314.4 W kg^{-1}.

2. Results and discussion

2.1 Characterizations of NMXC

Fig. 1a schematically illustrates the synthesis process of the crumpled N-doped MXene-based heterostructure through electrostatic self-assembly of MXene and melamine formaldehyde microspheres (denoted as MF) followed by pyrolysis. During the synthesis process, the formaldehyde, melamine, and formic acid catalyst were used to fabricate the MF microspheres template via a polymerization process.[30] And the delaminated conductive $Ti_3C_2T_x$ MXene with large flake size and plenty of surface hydrophilic functional groups such as –OH, –F, and –O was synthesized by selectively chemical etching Al atomic layers from MAX phase followed by liquid-phase exfoliating (Fig. S1, ESI†).[31] After that, the obtained $Ti_3C_2T_x$ MXene dispersion was added into the MF evenly dispersed colloidal suspension under stirring. The corresponding optical photographs of the reaction system show that the colour of the suspension changed from milk white to dark green immediately and quickly precipitated at the bottom of the beaker (left a transparent supernatant) (Fig. S2, ESI†). The different surface functional groups of the two components would generate strong electrostatic interaction, which lead to the spontaneously adsorbing of MF microspheres on the surface of $Ti_3C_2T_x$ MXene flakes upon the mixing process.[30] Then the as-obtained hetero-assembly sample (denoted as MXene/MF) was subjected to thermal annealing at 550 ℃ under argon atmosphere in order to simultaneously generate special 2D carbon configuration and nitrogen dopants of C_3N_4 due to the unique pyrolysis behaviour of melamine.[32] The pyrolysis process induces the MF template transformed into 2D carbon layer and covered on the surface of $Ti_3C_2T_x$ MXene. In addition, the employment of MF can also reduce the "dead volume" of $Ti_3C_2T_x$ MXene flakes by avoiding the layer-by-layer restacking problem and promote the nitrogen atoms doped into the $Ti_3C_2T_x$ MXene matrix.[33]

View Article Online
DOI: 10.1039/D1TA06974H

The characteristic morphologies of the prepared samples are examined by scanning electron microscopy (SEM) and transmission electron microscopy (TEM). As shown in Fig. 1b and S1 (ESI†), the as-prepared $Ti_3C_2T_x$ MXene nanosheets display a micron level lateral size and a 2D tulle-like laminar structure with abundant apparent wrinkles, indicating an ultra-thin structure of the $Ti_3C_2T_x$ nanosheets. As expected, $Ti_3C_2T_x$ MXene flakes uniformly and tightly wrap on the surface of the MF microspheres after mixing the two components together due to the static electricity (Fig. 1c). It can be observed that the resulting calcined sample turns into well-defined open interconnected frameworks with highly crumpled flakes and plenty of porosity after the pyrolysis process as confirmed by SEM and TEM images due to the reconstruction process from three-dimensional (3D) spheres of MF template to 2D flakes of N-doped carbon (NC) (Fig. 1d-f and Fig. S3c, ESI†), which is in sharp contrast with the relatively smooth morphology of $Ti_3C_2T_x$ nanosheets and MF (Fig. S3a-b, ESI†). The as-formed amorphous carbon and crumpled structure would effectively inhibit the "face-to-face" restacking problems of $Ti_3C_2T_x$ MXene sheets. The close observation in the high-resolution TEM (HRTEM) image clearly verifies that a layer of amorphous carbon tightly attaches on the surface of $Ti_3C_2T_x$ MXene nanosheets (marked by green dashed line in Fig. 1g), which can act as the oxidation-resistive layer during the charge storage process and effectively strengthen its electrochemical stability.[25] The diffraction rings in the selected area electron diffraction (SAED) patterns in Fig. 1h clearly manifests a polycrystalline property of NMXC. The apparent lattice fringes with an interlayer distance of 1.28 nm correspond to the (002) crystalline plane of the $Ti_3C_2T_x$ MXene (Fig 1i).[34] The representative AFM image and its thickness profile in Fig. 1j and k show a very thin NMXC flake with an average thickness of around 3.6-5.5 nm. The corresponding element mapping images of the NMXC nanohybrid in Fig. 1l and Fig. S3d (ESI†) reveal the even distribution of C, O, N, and Ti. It is noteworthy that the distribution of nitrogen element is relatively homogeneous throughout the whole composite including the carbon skeleton and MXene matrix rather than concentrated at the carbon component, further manifesting a homogenous nitrogen doping effect into the MXene (Fig. 1l). The EDX spectrum of the NMXC sample in Fig. S4 (ESI†) also confirms the co-existence of C, O, N, and Ti elements. The above results clearly demonstrate that the template-induced process can synergistically construct 3D interpenetrated frameworks, yield a protective layer, and facilitate the nitrogen doping, which effectively suppress the restacking of delaminated MXene flakes, expose more electroactive sites, and promote the transfer of electrolyte ions for energy storage.

The crystal structures of the prepared samples are characterized by X-ray diffraction (XRD) analysis. The XRD patterns of $Ti_3C_2T_x$ MXene, NMXC, and NC samples are displayed in Fig. 2a-b. It can be observed that the (002) characteristic diffraction peak shifts from 7.9° of pure $Ti_3C_2T_x$ MXene to 6.7° for NMXC, corresponding to the increase in interlayer spacing from 1.12 to 1.32 nm (calculated from Bragg's Law) due to the N doping effect during the reconstruction process (Fig. 2a-b). The obtained results are in consistent with the HRTEM analysis. The observable increased interlayer spacing of MXene might possibly result from the larger atomic radius of nitrogen heteroatom than carbon element in the MXene matrix.[30,35,36] Additionally, previous works have demonstrated that the doped nitrogen would further enhance the electrical conductivity while the enlarged interlayer spacing promotes the intercalation, which are beneficial for boosting the electrochemical properties of MXene based materials.[30] Meanwhile, the NMXC sample also possesses the characteristic (002) peak pertaining to NC at 26.3°, which are indicative of the formation of hybrid heterostructure. Interestingly, the (004) diffraction peak between 15 and 20° of MXene for NMXC composite disappears in XRD pattern, which can be ascribed to the bending of the $Ti_3C_2T_x$ sheets and the random orientation of the crumpled structure.[37,38,39] The XRD patterns exhibit no obviously characteristic peak of TiO_2, which further certify the protection (anti-oxidation) ability of carbon layer.

In order to further probe the electronic structures of the prepared MXene, NMXC, and NC samples, X-ray photoelectron spectroscopy (XPS) tests are performed. It can be observed that the survey spectrum for NMXC and NC samples in Fig. 2c emerges the characteristic peaks of N 1s compared with the pure MXene, confirming the successful nitrogen doping for the NMXC sample. The deconvoluted peaks located at 396.7, 398.7, and 400.4 eV of the N 1s spectrum in Fig. 2d correspond to the Ti−N in MXene, pyridinic N and pyrrolic N species in N-doped carbon, respectively, which are consistent with the previous reported N-doped $Ti_3C_2T_x$ composites.[40,41] The C 1s spectrum in Fig. 2e for NMXC also corroborates the nitrogen dopants are incorporated into the $Ti_3C_2T_x$ matrix. The C 1s spectrum for NMXC can be deconvoluted into four peaks at 282, 284.8, 285.6, and 286.7 eV, which can be accordingly assigned to the C-Ti, C-C, C-N, C-O species, respectively.[42-45] The Ti 2p spectrum of NMXC is shown in Fig. 2f. Two peaks at 457.2 and 464.3 eV correspond to TiO_2 species.[46,47]

View Article Online
DOI: 10.1039/D1TA06974H

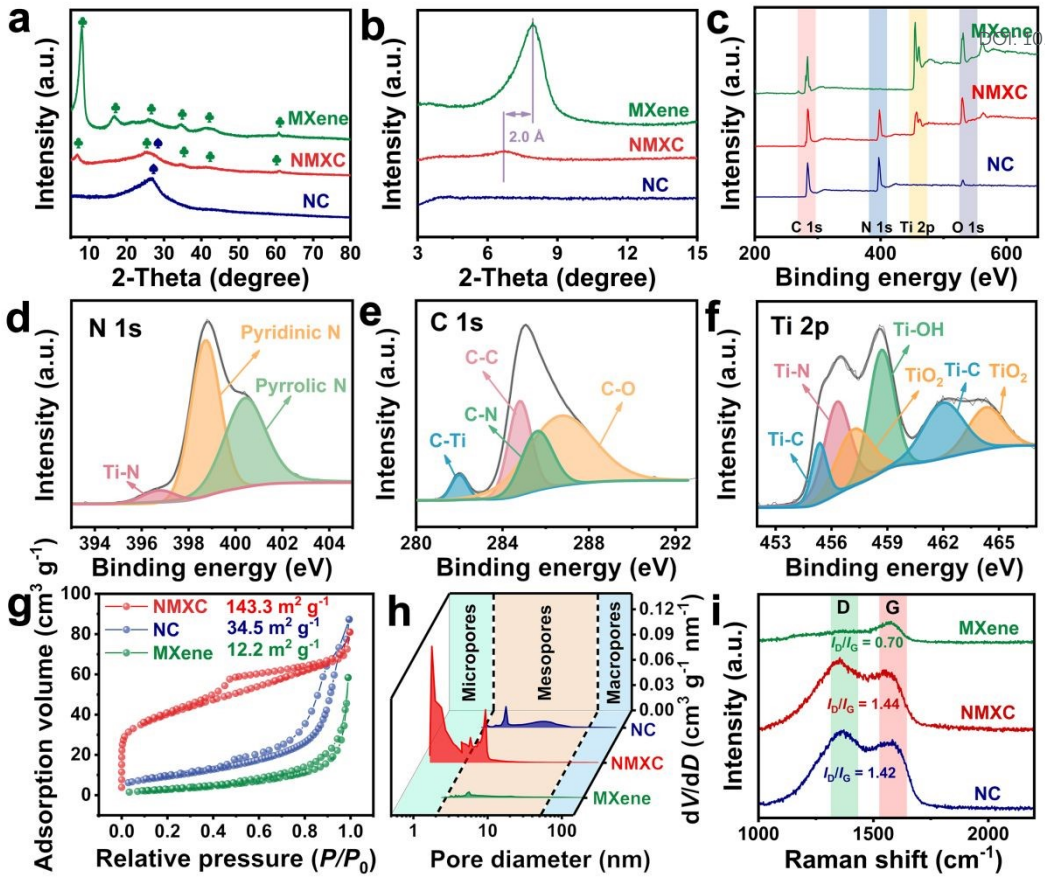

Fig. 2 (a) XRD and (b) magnified XRD patterns of MXene, NC and NMXC. (c) XPS survey spectra of MXene, NC and NMXC. XPS survey spectra of NMXC at (d) N 1s, (e) C 1s, (f) Ti 2p regions. (g) N_2 adsorption/desorption isotherms. (h) BJH and HK pore size distribution. (i) Raman spectra of MXene, NC and NMXC.

The fact that the TiO_2 $2P_{3/2}$ at 457.2 eV of NMXC can be traced in the XPS spectrum, which may originate from the slight oxidation due to the existence of abundant hydroxyl groups on the surface of $Ti_3C_2T_X$ flakes.[37,47-54] The peaks centred at 455.3 (Ti $2p_{3/2}$) and 462 eV (Ti $2p_{1/2}$) correspond to the Ti-C bond.[55] The rest peaks located at 456.3 and 458.7 eV confirm the existence of Ti-N and Ti-OH.[47] The obtained results reveal that the nitrogen was successfully doped into the $Ti_3C_2T_x$ skeleton.

In addition, Fig. 2g and h display the N_2 adsorption/desorption isotherm and pore size distribution of the prepared samples. Fig. 2g exhibits type I and IV mixed isotherm. The sharply increased adsorption volume at low relative pressure (P/P_0 < 0.1) and the obvious hysteresis loop corroborates the micropore/mesoporous dominant structure of NMXC. The corresponding Brunauer-Emmett-Teller (BET) specific surface area is 143.3 m^2 g^{-1}, and the total pore volume and micropore volume based on Barrett-Joyner-Halenda (BJH) and Horvath-Kawazoe (HK) methods are 0.11 and 0.06 cm^3 g^{-1}, respectively. The specific surface area of NMXC is much larger than NC (34.5 m^2 g^{-1}) and pure MXene (12.2 m^2 g^{-1}), implying the "face-to-face" restacking is effectively inhibited. As shown in Fig. S5a-c (ESI†), the surface wettability of NMXC still maintains the inherent hydrophilicity from pure MXene (22.3°) and NC (49.1°) with a water contact angle of 58.0°. The increased water contact angle can be ascribed to the partially removal of the hydrophilic group (*e.g.*, -OH terminations) at higher calcination temperature and the contribution to hydrophobicity from the rough surface and crumpled flakes of NMXC.[56,57]

Raman spectra are further used to reveal the structural characteristics of NMXC. As shown in Fig. 2i, the representative peaks at approximately 1369 and 1573 cm^{-1} can be assigned to the D band (is caused by disordered or defect structure) and G band (results from graphite structure), respectively. The intensity ratio for I_D/I_G of MXene is 0.70. The corresponding I_D/I_G values of NC and NMXC are 1.42 and 1.44, respectively, which implies more disordered and defective structures of NMXC compared with MXene after the incorporation of nitrogen doping and amorphous carbon layer wrapping.[58] Thermogravimetric analysis (TGA) of NMXC is also performed in an air atmosphere. As shown in Fig. S6 (ESI†), the content of NC in NMXC was approximately 71.6% of the initial weight in the composite.

2.2 Electrochemical properties of Zn//NMXC ZHSC in aqueous electrolyte

View Article Online
DOI: 10.1039/D1TA06974H

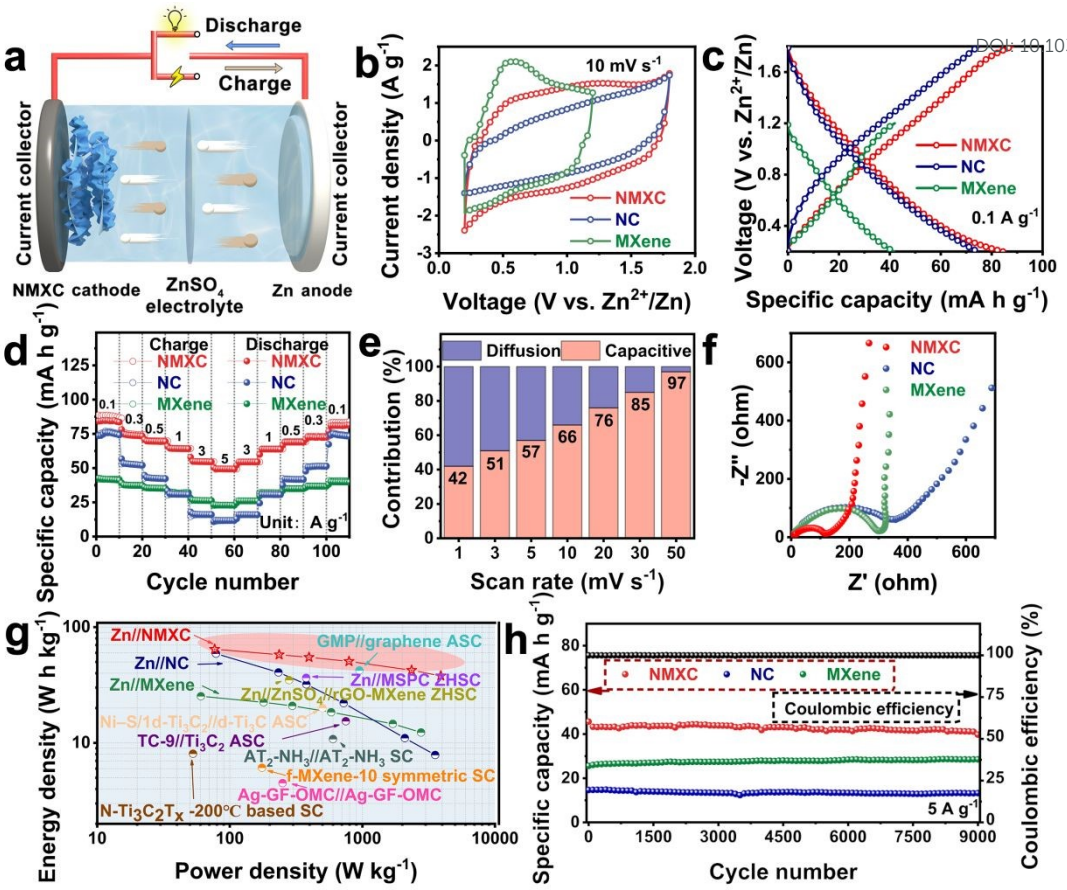

Fig. 3 The electrochemical performances of Zn//MXene, Zn//NC and Zn//NMXC ZHSCs in aqueous $ZnSO_4$ electrolyte. (a) Schematic of an aqueous Zn//NMXC ZHSC device. (b) CV profiles of Zn//MXene, Zn//NC, and Zn//NMXC ZHSCs at 10 mV s^{-1}. (c) GCD profiles at 0.1 A g^{-1}. (d) Rate capability of the as-designed ZHSCs. (e) The capacitive and diffusion contribution ratios to the total capacity at different scan rates for Zn//NMXC ZHSC. (f) EIS plots of Zn//MXene, Zn//NC, and Zn//NMXC ZHSCs. (g) Ragone plot of the as-designed ZHSCs compared with other energy storage devices. (h) Cycling performances of Zn//MXene, Zn//NC, and Zn//NMXC ZHSCs, and Coulombic efficiency of Zn//NMXC ZHSC.

To reveal the energy storage properties of the as-made NMXC, a typical aqueous ZHSC (referred to as Zn//NMXC ZHSC hereafter) was fabricated by using the Zn foil anode (0.08 mm in thickness), NMXC cathode, and 2 M $ZnSO_4$ aqueous electrolyte (Fig. 3a). Fig. 3b exhibits the cyclic voltammetry (CV) curves at a sweep rate of 10 mV s^{-1} for Zn//MXene (an aqueous ZHSC with a $Ti_3C_2T_x$ MXene film cathode), Zn//NC (an aqueous ZHSC with a NC cathode), and Zn//NMXC ZHSC. Notably, it can be observed that the Zn//NMXC ZHSC was able to reversibly operate within a wider voltage range from 0.2 to 1.8 V, which is substantially larger than the voltage window of the pure $Ti_3C_2T_x$ MXene based Zn//MXene ZHSC (0.2-1.2 V, further increasing the voltage window leads to polarization phenomenon, Fig. S7, ESI†). Similar result is also found in the linear sweep voltammetry (LSV) curves (Fig. S8, ESI†). This finding clearly verifies that the as-formed amorphous carbon layer enhances the electrochemical stability of MXene and protects the MXene from being oxidized at positive potential. In addition, the area of the enclosed CV curves for Zn//NMXC ZHSC is obviously larger than that of Zn//NC ZHSC, revealing that the amorphous carbon layer attached to the $Ti_3C_2T_x$ MXene enhances the charge storage ability of NC that perhaps results from the incorporating of highly conductive $Ti_3C_2T_x$ MXene inside. The Zn//MXene ZHSC exhibits slight redox peaks that deviated from the ideal rectangular shape, experimentally verifying the existing of pseudocapacitive behaviour for the MXene cathode.[59] It can be observed that the CV curves for Zn//NMXC ZHSC possess the approximately symmetrical rectangular shape with relatively flat curves without obviously redox behaviours compared with Zn//MXene (emerge weak redox peaks) and Zn//NC ZHSCs, revealing an enhanced reversibility of the NMXC heterostructure due to the synergistically interplayed effect of the boosted electronic conductivity, amorphous carbon wrapping, larger interlayer spacing, and the incorporation of N atoms. The *ex-situ* XRD spectra were also adopted at the selected five states to explore the structural changes of the NMXC cathode and Zn anode in aqueous ZHSC during the electrochemical charge storage process (Fig. S9, ESI†). The charge process for the as-designed ZHSC involves the SO_4^{2-} anions migrate to the surface of NMXC cathode

View Article Online
DOI: 10.1039/D1TA06974H

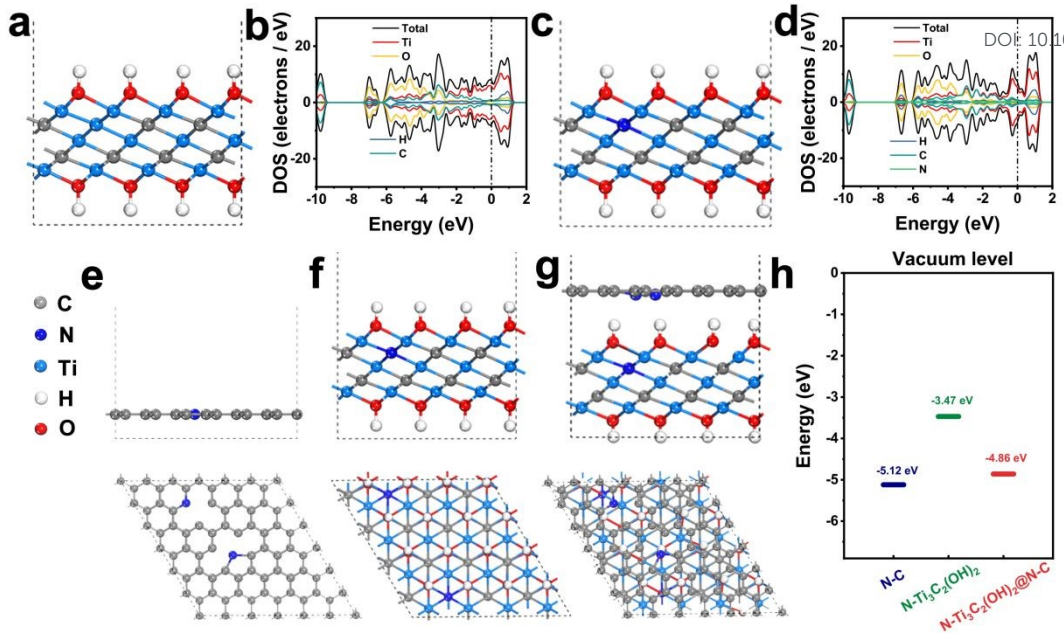

Fig. 4 Schematic diagram of the (a) OH-terminated $Ti_3C_2(OH)_2$ and (c) N-$Ti_3C_2(OH)_2$ models. DOS diagrams of (b) OH-terminated $Ti_3C_2(OH)_2$ and (d) N-$Ti_3C_2(OH)_2$. Side and top views of (e) N-C, (f) N-$Ti_3C_2(OH)_2$, and (g) N-$Ti_3C_2(OH)_2$@N-C. (h) WF of N-C, N-$Ti_3C_2(OH)_2$, and N-$Ti_3C_2(OH)_2$@N-C.

via the physically adsorbing process to form the electric double layer capacitor (EDLC), meanwhile, the Zn^{2+} cations move to the Zn anode to generate the metallic zinc. During the discharge process, the SO_4^{2-} anions and Zn^{2+} cations move to the opposite direction and reversed electrochemical reaction occurs.[60]

The galvanostatic charge/discharge (GCD) characteristics of Zn//MXene, Zn//NC, and Zn//NMXC ZHSCs were further investigated. The GCD curves in Fig. 3c for Zn//NMXC ZHSC exhibit a typical symmetrical shape, suggesting an excellent reversibility of NMXC. Accordingly, as shown in Fig. 3c, the GCD curves for Zn//NMXC ZHSC exhibit a higher specific capacity at 0.1 A g^{-1} compared with the Zn//MXene and Zn//NC ZHSC counterparts. Meanwhile, the wider operation voltage range of Zn//NMXC ZHSC in comparison with the Zn//MXene device further proves the enhanced resistance to electrochemical oxidation at positive potential and superior electrochemical performance of the heterogeneous NMXC sample.

Fig. 3d shows that the Zn ion storage capacities of Zn//NMXC invariably exceed its ZHSC counterparts at current densities from 0.1 to 5 A g^{-1}. A maximum specific capacity of 83.9 mA h g^{-1} at 0.1 A g^{-1} with retention rate of 58.8% at 5 A g^{-1} was obtained for Zn//NMXC, which is substantially superior than Zn//NC (75.0 mA h g^{-1} with 15.7% capacity retention) and Zn//MXene (41.5 mA h g^{-1} with 55.2% capacity retention) ZHSCs. Note that a reversible discharge capacity of 81.4 mA h g^{-1} for Zn//NMXC is obtained, equivalent of 97% of the initial capacity value as the current density recovers back to 0.1 A g^{-1}, indicating an enhanced electron/ion transfer ability, lower resistance, fast kinetics response, and high reversibility of NMXC.

The diffusion and capacitive contributions were further distinguished by the current/charge response of CV curves according to the Dunn's method.[61, 62]

$$i\,(\mathrm{V}) = i_{\mathrm{cap}} + i_{\mathrm{diff}} = k_1 v + k_2 v^{1/2} \quad (1)$$

where $k_1 v$ and $k_2 v^{1/2}$ represent the capacitive and diffusion contributions, respectively. Fig. 3e and Fig. S10 (ESI†) show that the relative capacitive contribution ratio increases and the diffusion contribution ratio decreases when the scan rates raised, and the calculated capacitive contribution ratio is 42% at 1 mV s^{-1} and gradually dominates the total stored capacity (97%) as the scan rates further change to 50 mV s^{-1}, which indicates a capacitive-controlled kinetic at fast scan rates. The above results suggest that the interpenetrating structure and the MXene component would offer effective pathways for rapid ion diffusion and electron transfer.[63]

Fig. 3f displays the electrochemical impedance spectra (EIS) of Zn//MXene, Zn//NC, and Zn//NMXC ZHSCs. The diameter of the semicircle at high-frequency regions is proportional to the charge transfer resistance (R_{ct}) while the slope in low-frequency regions relates to the Zn ion diffusion process. Obviously, Zn//NMXC ZHSC possesses smaller semicircle diameter and more vertical lines, implying that the NMXC is more beneficial for charge transfer and ion diffusion at the electrode/electrolyte interface compared with MXene and NC.[5] More encouragingly, the aqueous Zn//NMXC ZHSC exhibits a superior energy density of 64.5 W h

kg^{-1} and a maximum power density of 3.9 kW kg^{-1} (Fig. 3g). The obtained energy density is higher than the Zn//MXene and Zn//NC ZHSCs, and even outperforms many of the reported energy storage systems, such as Zn//$ZnSO_4$//rGO-MXene ZHSC (34.9 W h kg^{-1} at 279.9 W kg^{-1}), [6] N-$Ti_3C_2T_x$-200 ℃ based SC (8.07 W h kg^{-1} at 52.8 W kg^{-1}), [33] AT_2-NH_3//AT_2-NH_3 SC (10.8 W h kg^{-1} at 600 W kg^{-1}), [43] Zn//MSPC ZHSC (36.5 W h kg^{-1} at 376.6 W kg^{-1}), [64] TC-9//Ti_3C_2 ASC(15.4 W h kg^{-1} at 750 W kg^{-1}), [65] Ag-GF-OMC//Ag-GF-OMC (4.5 W h kg^{-1} at 250 W kg^{-1}), [66] Ni–S/1d-Ti_3C_2//d-Ti_3C ASC (20 W h kg^{-1} at 0.5 kW kg^{-1}), [67] GMP//graphene ASC (42.3 W h kg^{-1} at 950 W kg^{-1}), [68] f-MXene-10 symmetric SC (6.1 W h kg^{-1} at 175 W kg^{-1}). [69]

Remarkable, the Zn//MXene, Zn//NC, and Zn//NMXC ZHSCs also deliver excellent cycling stabilities as revealed in Fig. 3h. 87.1% capacity retention of Zn//NMXC ZHSC can be obtained at 5 A g^{-1} after 9000 charge/discharge terms along with >99% exceptional Coulombic efficiency, implying a highly rechargeable feature and the good structure stability. The *ex-situ* XRD measurement of the NMXC cathode was further performed to confirm the structural stability after cycling. As shown in Fig. S11 (ESI†), the main peaks for NMXC are maintained after prolonged electrochemical testing (*e.g.*, the (002) peak of MXene and the (002) peak of NC). Besides that, only the characteristic diffraction peaks of PTFE (JCPDS No. 54-1595), and $ZnSO_4{\cdot}6H_2O$ (JCPDS No. 32-1478), and $Zn_4SO_4(OH)_6{\cdot}H_2O$ (JCPDS No. 39-0690) byproducts can be observed in the XRD pattern without obvious signals of TiO_2, indicating a desirable electrochemical stability of NMXC in aqueous ZHSC. The above-mentioned results suggest that the electrochemical performance for MXene in ZHSC can be substantial enhanced by engineering interpenetrating framework with amorphous carbon coating and N-doping.

2.3 Density functional theory (DFT) calculations

To reveal the N dopants for improving the electronic conductivity of MXene and the carbon coating for enhancing the oxidation resistance ability under anodic process of NMXC, DFT simulation calculations were conducted. Considering that previous works have demonstrated that the OH was the main terminal group,[21] OH terminated $Ti_3C_2(OH)_2$ model with part of C position substituted by N atom (denoted as N-$Ti_3C_2(OH)_2$) was adopted for simplicity (Fig. 4a and c). The density of states (DOS) for $Ti_3C_2(OH)_2$ with or without N substitution are both calculated for comparison (Fig. 4a-d). As shown in Fig. 4a-d, the electron density obtained from the integration of electronic DOS within a range of -10 to 2 at the Fermi level for $Ti_3C_2(OH)_2$ and N-$Ti_3C_2(OH)_2$ are 11.98 and 14.29, respectively, which reveals more free electrons that generates in the system and results in an effective increase of electronic conductivity for N-$Ti_3C_2(OH)_2$.[70] The above results indicates that the N-doping effect boosts the electrical conductivity of MXene matrix.[33] In addition, previous work has demonstrated that the work function (WF) is direct proportional of the ability to withstand anodic oxidation and electron loss, and therefore, the WF was also used for further qualitatively estimating the stability during the electrochemical process.[21] Fig. 4e-g display the optimized geometric configurations of N-doped carbon (denoted as N-C), N-$Ti_3C_2(OH)_2$, and N-$Ti_3C_2(OH)_2$@N-C, respectively. The N-C possesses the highest WF of 5.12 eV among the three samples (Fig. 4h). As expected, after compositing with N-C, the WF increases from 3.47 eV of N-$Ti_3C_2(OH)_2$ to 4.86 eV for N-$Ti_3C_2(OH)_2$@N-C as the Fermi level shift, revealing a higher ability to withstand the electron loss and a wider positive potential window. The obtained results suggest that the combination of inorganic or organic materials with higher WF would widen the operating potential of MXene and enhance its oxidation resistance under high positive potentials.

2.4 Characterizations of the PAM-co-PAA/κ-CG/$ZnSO_4$ hydrogel/electrolyte

Fig. 5a illustrates the fabrication process of the PAM-co-PAA/κ-CG hydrogel. Briefly, certain amount of acrylamide monomer (AM), acrylic acid monomer (AA), 2-hydroxy-4′-(2-hydroxyethoxy)-2-methylpropiophenone ultraviolet (UV)-initiator, N,N′-methylenebisacrylamide (MBAA) crosslinker, and KCl ionic crosslinker were dispersed in deionized water at room temperature, followed by adding κ-CG at 60 ℃ to form a uniform colloid. In the subsequent cooling process, a physically ionic crosslinked κ-CG first network was formed due to the generation of the κ-CG double helices structure with the assistance of KCl. Under the following UV light irradiation, an *in-situ* photopolymerization process was triggered in the presence of UV-initiator and MBAA crosslinker, which produces PAM-co-PAA copolymer networks.[71] Meanwhile, the amide group on PAM-co-PAA chain and hydroxyl groups of κ-CG chains would generate the inter-molecular hydrogen bonds by macromolecular chains rearrangement together with chain entanglements between them.[72,73,74] The synergetic effects of the chemically covalent and physically ionic double crosslinked domains as well as the physical entanglements are responsible for the stretchability and mechanical properties. In addition, the inter-molecular hydrogen bonds would facilitate the dynamical recombination under stress condition, homogenize the polymer

View Article Online
DOI: 10.1039/D1TA06974H

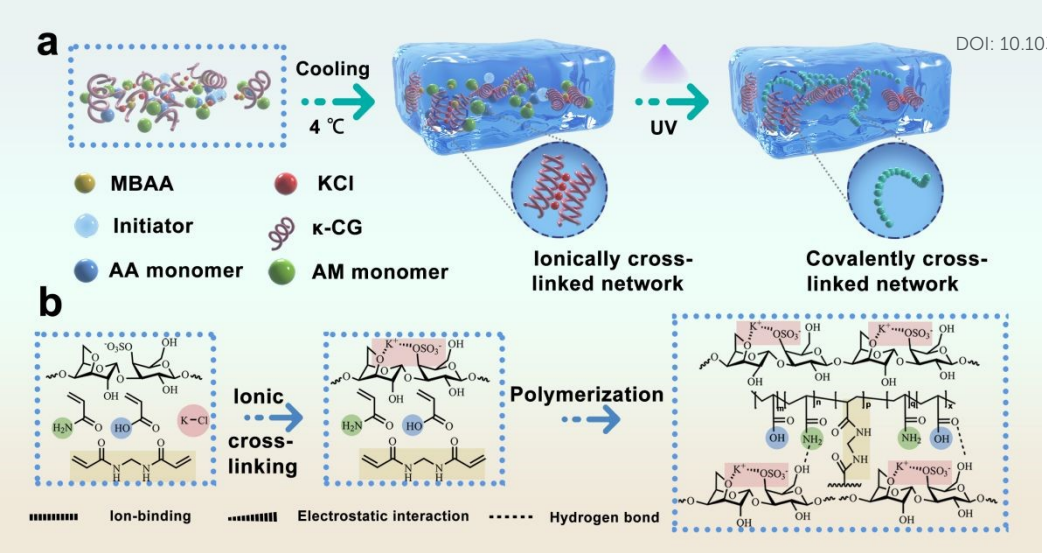

Fig. 5 (a) Synthetic schematic and (b) internal structure of the PAM-co-PAA/κ-CG hydrogel.

dual network, and generate satisfactory stretchability and compressibility (Fig. 5b).[75]

Subsequently, the PAM-co-PAA/κ-CG hydrogel was soaked into 2 M $ZnSO_4$ aqueous solution to absorb sufficient electrolyte ion for forming the zinc-ion-conducting hydrogel/electrolyte. A superb adsorbed electrolyte capacity of about 1.22 g was obtained that is about 3.9 times of the initial hydrogel mass (0.31 g) after 12 h. The volume further changes to several times of the initial one after absorbing the electrolyte (Fig. S12a and b, ESI†). In addition, a similar adsorbed electrolyte capacity of 1.23 g was obtained for the PAM-co-PAA hydrogel with the initial hydrogel mass of 0.30 g, revealing that the absorbing capacity for the PAM-co-PAA/κ-CG hydrogel mainly roots in the PAM-co-PAA matrix.

The morphology features of the hydrogel at dry state were further revealed by the SEM image. As shown in Fig. 6a, the freeze-dried PAM-co-PAA/κ-CG hydrogel displays interpenetrated and intertwining porous structure with abundant channels, which would provide sufficient ion migration paths and enhanced water-retention ability. The chain structures of the κ-CG, PAM-co-PAA, and PAM-co-PAA/κ-CG hydrogels are further evaluated by the Fourier transform infrared spectroscopy (FTIR) as shown in Fig. 6b. The characteristic peaks of PAM-co-PAA (blue line) are located at about 3343, 3199, 2935, 1657, 1618, 1451, and 1414 cm^{-1}, which correspond to the N-H stretching vibration, N-H stretching, C-H stretching vibration, C=O stretching, N-H deformation of primary amine, CH_2 in-plane scissoring, and C-N stretching vibration of primary amide, respectively.[76-79] The absorption bands of κ-CG at 3402, 2952, 1642, 1427, 1374, 1233, 1158, 1070, 929, and 846 cm^{-1} relate to the O-H stretching, C-H stretching, asymmetric vibration of -COO-, C-O-H in-plane bending vibration, C-H bending vibration, O=S=O symmetric vibration, bridge -O stretching, C-O stretching, C–O–C in 3, 6-anhydro-D-galactose, and C_4-O-S stretching vibration, respectively.[73,80,81] Moreover, the signals located at 929, 846, 3343, 3199, 1657, and 1618 cm^{-1} appear in the FTIR spectra of PAM-co-PAA/κ-CG, which correspond to the characteristic vibration of κ-CG and PAM-co-PAA, respectively, indicating the successful synthesis of PAM-co-PAA/κ-CG hybrid hydrogel. Besides, the shift of O–H stretching to lower wave-numbers further certifies the appearance of hydrogen bond between κ-CG and PAM-co-PAA.[73,74]

The ion conductivity of PAM-co-PAA/κ-CG/$ZnSO_4$ zinc-ion-conducting hydrogel/electrolyte was evaluated by the EIS measurement based on the following equation:[82, 83]

$$\sigma = \frac{L}{AR} \quad (2)$$

where σ (S m^{-1}), L (m), R (Ω), and A (m^2) represent the ionic conductivity, thickness, resistance, and test area of the hydrogel/electrolyte, respectively. To further reveal the ionic conductivity of the double crosslinked PAM-co-PAA/κ-CG/$ZnSO_4$ hydrogel/electrolyte, PAM-co-PAA/$ZnSO_4$ was also tested for comparison. The calculated ionic conductivity is 1.76 S m^{-1} (based on a PAM-co-PAA/κ-CG/$ZnSO_4$ hydrogel/electrolyte with the size of 10×10×1.5 mm^3 and an ohmic resistance value of 8.6 Ω), which is higher than the ionic conductivity (1.50 S m^{-1}) of PAM-co-PAA/$ZnSO_4$, revealing that the κ-CG component enhances the ionic conductivity of the hybrid hydrogel that possibly results from

View Article Online
DOI: 10.1039/D1TA06974H

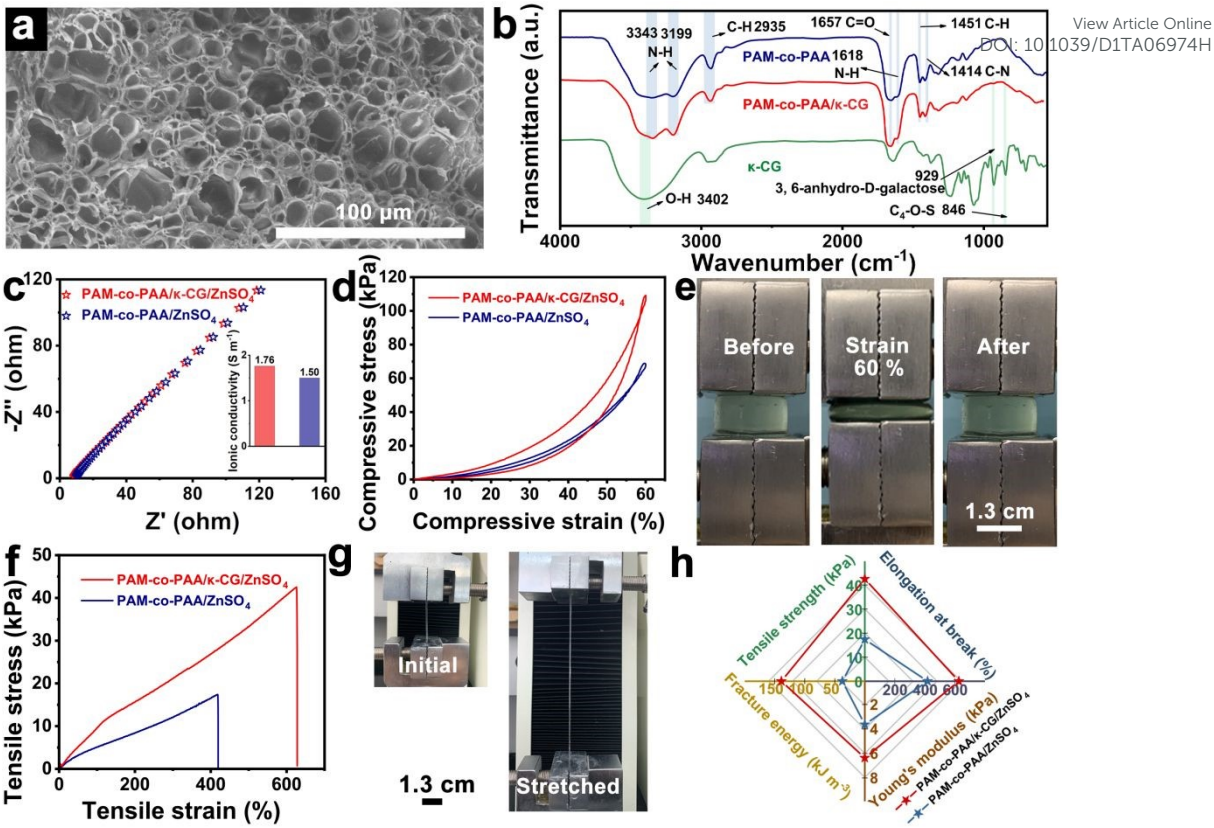

Fig. 6 The characterization of the prepared hydrogel. (a) SEM image of the freeze-dried PAM-co-PAA/κ-CG hydrogel. (b) FTIR spectra of the κ-CG, PAM-co-PAA, and PAM-co-PAA/κ-CG hydrogels. (c) EIS spectra of PAM-co-PAA/κ-CG/$ZnSO_4$ and PAM-co-PAA/$ZnSO_4$ hydrogel/electrolytes and the corresponding ionic conductivities. Mechanical properties: (d) Compression curves of the PAM-co-PAA/κ-CG/$ZnSO_4$ and PAM-co-PAA/$ZnSO_4$ hydrogel/electrolytes. (e) Pictures demonstrating the compression process of the PAM-co-PAA/κ-CG/$ZnSO_4$ hydrogel/electrolyte. (f) Tensile stress-strain curves of the PAM-co-PAA/κ-CG/$ZnSO_4$ and PAM-co-PAA/$ZnSO_4$ hydrogel/electrolytes. (g) Optical images demonstrating the stretching ability of the PAM-co-PAA/κ-CG/$ZnSO_4$ hydrogel/electrolyte. (h) Comparison of the mechanical properties in terms of tensile strength, elongation at break, fracture energy, and Young's modulus of PAM-co-PAA/κ-CG/$ZnSO_4$ and PAM-co-PAA/$ZnSO_4$ hydrogel/electrolytes.

the charged sulphate functional groups of κ-CG chain (Fig. 6c).

The PAM-co-PAA/κ-CG/$ZnSO_4$ hydrogel/electrolyte also exhibits desirable flexibility. It can be observed in Fig. S12c-f (ESI†) that the hydrogel displays shapable properties and can be easily folded, rolled, or can resist a weight of 20 g without any obvious fractures, proving its exceptional softness. The mechanical properties of PAM-co-PAA/κ-CG/$ZnSO_4$ were further investigated by the loading-unloading compression tests under a compressive strain of 60%. A pronounced hysteresis loop was observed for PAM-co-PAA/κ-CG/$ZnSO_4$ compared with PAM-co-PAA/$ZnSO_4$ in the loading-unloading curves of Fig. 6d, suggesting a gradual internal fracture process. [84] In addition, the pronounced hysteresis loop also reveals that the energy dissipation for PAM-co-PAA/κ-CG/$ZnSO_4$ under loadings highly relies on the rupture of the ionic crosslinked κ-CG network. Additionally, the corresponding photograph exhibits that the PAM-co-PAA/κ-CG/$ZnSO_4$ hydrogel/electrolyte is sufficiently robust to endure the compression and fully recovers without obvious deformation or fracture after withdrawing the external force under the same strain of 60%, which demonstrates the self-recoverability of the double crosslinked network after unloading (Fig. 6e).

The tensile stress-strain curve of the PAM-co-PAA/κ-CG/$ZnSO_4$ hydrogel/electrolyte also demonstrates that the tensile property was greatly depended on the κ-CG component. As shown in Fig. 6f, the fracture strength (42.5 kPa) and fracture energy (138.9 kJ m^{-3}) of PAM-co-PAA/κ-CG/$ZnSO_4$ hydrogel/electrolyte are obviously enhanced compared with PAM-co-PAA/$ZnSO_4$. A higher fracture strain over 626.0% for PAM-co-PAA/κ-CG/$ZnSO_4$ compared with the hydrogel without κ-CG (418.3%) reveals a boosted tensile property. The corresponding optical images demonstrate a high stretch ability of the PAM-co-PAA/κ-CG/$ZnSO_4$ hydrogel/electrolyte (Fig. 6g). Moreover, the PAM-co-PAA/κ-CG/$ZnSO_4$ hydrogel/electrolyte also exhibits higher tensile strength (42.5 kPa), elongation at break (626.0%), fracture energy (138.9 kJ m^{-3}), and Young's modulus (6.4 kPa) compared with the PAM-co-PAA/$ZnSO_4$ hydrogel/electrolyte with smaller tensile strength (17.4 kPa), elongation at break (418.3%), fracture energy (37.5 kJ m^{-3}), and Young's modulus (3.6 kPa) (Fig. 6h). The satisfactory

View Article Online
DOI: 10.1039/D1TA06974H

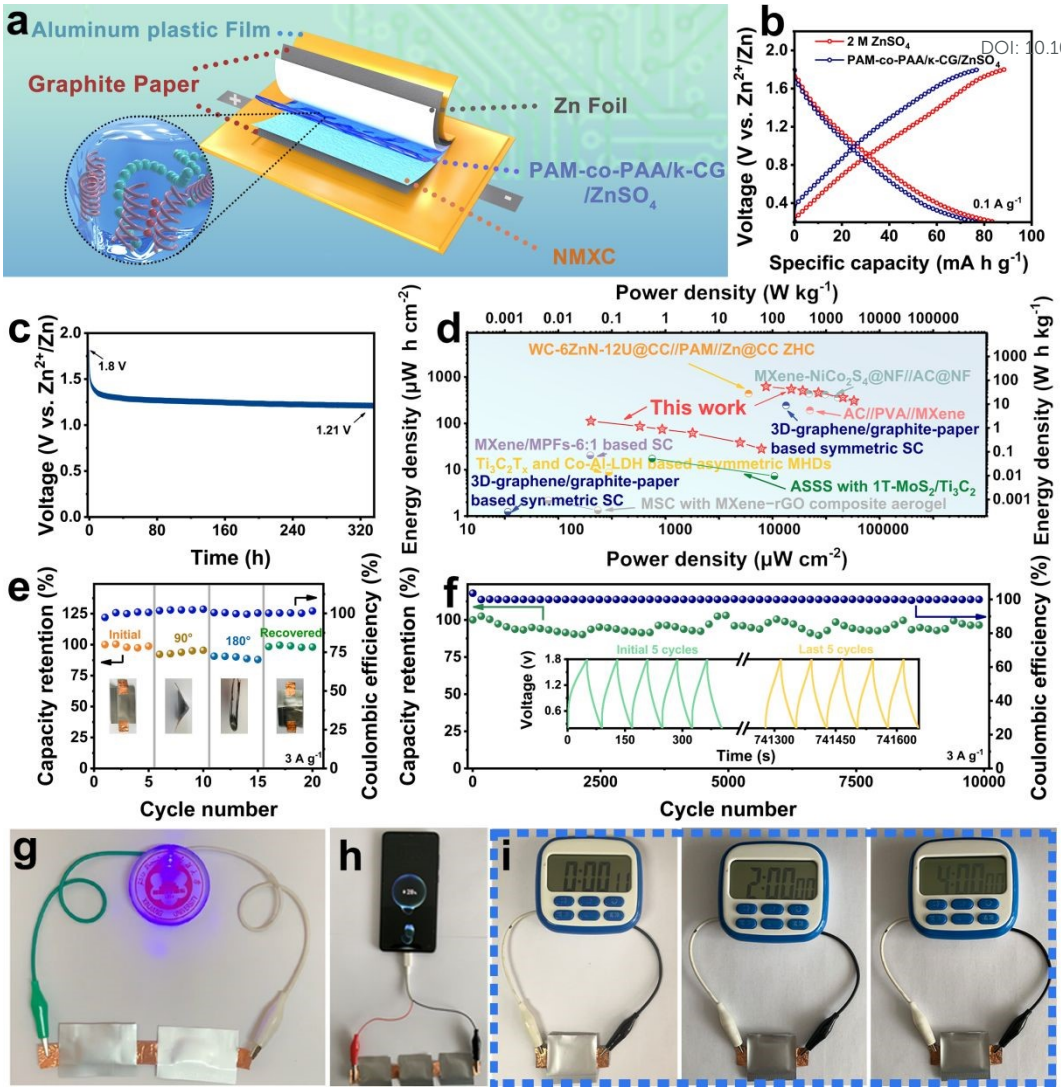

Fig. 7 (a) Schematic of the quasi-solid-state Zn//NMXC ZHSC with the PAM-co-PAA/κ-CG/$ZnSO_4$ hydrogel/electrolyte. (b) GCD curves of ZHSCs in aqueous electrolyte and hydrogel/electrolyte at 0.1 A g^{-1}. (c) The self-discharging curve of the quasi-solid-state ZHSC. (d) The Ragone plots of the quasi-solid-state ZHSC and other energy storage devices. (e) Capacity retention of the quasi-solid-state ZHSC under bending conditions. (f) Cycling stability and Coulombic efficiency at 3 A g^{-1} of the quasi-solid-state ZHSC, inset shows the initial five cycles and last five cycles. Photographs demonstrate that (g) a LED lamp, (h) a mobile phone, (i) a calculagraph driven by the quasi-solid-state ZHSC.

mechanical properties of the PAM-co-PAA/κ-CG/$ZnSO_4$ zinc-ion-conducting hydrogel/electrolyte result from the synergistic effect of the physical-ionic/chemical-covalent dual crosslinked networks and κ-CG toughening association mechanism. The ionically crosslinked double-helix matrix of κ-CG unzipped itself progressively and even dynamically break or recover to protect the main rigid framework of PAM-co-PAA from being broken during the deformation process, which would boost the toughness of the hydrogel via dissipating mechanical energy.[85] Besides, the chains entanglements and hydrogen bonds between the two networks also help strengthen the mechanical properties.[71] Moreover, considering that no water seepage phenomenon was generated during the mechanical deformation process of the hydrogel, revealing that the $ZnSO_4$ electrolyte was well confined in the PAM-co-PAA/κ-CG hydrogel matrix.

2.5 Electrochemical properties of the quasi-solid-state Zn//NMXC ZHSC

The superior mechanical properties and satisfactory ionic conductivity endow the PAM-co-PAA/κ-CG/$ZnSO_4$ hydrogel as potential zinc-ion-conducting electrolyte for quasi-solid-state ZHSCs.[86] To verify the practicability of the as-fabricated NMXC and PAM-co-PAA/κ-CG/$ZnSO_4$, a soft-package quasi-solid-state ZHSC was assembled by using the Zn foil anode and the prepared NMXC cathode (graphite paper as current collector) with the as-design hydrogel/electrolyte as illustrated in Fig. 7a. The photograph of the quasi-solid-state ZHSC is displayed in Fig. S13 (ESI†). Experimentally, the charge storage properties of the quasi-solid-

View Article Online
DOI: 10.1039/D1TA06974H

state ZHSC are revealed by CV, GCD, and long-term cycling tests. The CV profiles at various scan rates in Fig. S14 (ESI†) demonstrate that the quasi-solid-state ZHSC assembled by the PAM-co-PAA/κ-CG/$ZnSO_4$ hydrogel/electrolyte can be rechargeable in a voltage range of 0.2-1.8 V. Notably, these CV curves for the quasi-solid-state ZHSC system possess the same voltage window and semblable CV shapes as the aqueous device without obvious electrochemical polarization, revealing the analogical energy storage mechanism compared with the aqueous system. Consistently, the GCD curves in Fig. 7b of the quasi-solid-state ZHSC exhibits a discharge capacity of 72.5 mA h g^{-1} at a current density of 0.1 A g^{-1}. The obtained value is comparable with the aqueous ZHSC, demonstrating a remarkable zinc storage property for NMXC in PAM-co-PAA/κ-CG/$ZnSO_4$. The GCD curve approximately displays linearly relation without potential plateaus, revealing an EDLC charge storage mechanism for NMXC in the quasi-solid-state system.[87] Additionally, the charge and discharge parts for the GCD curve are almost symmetric with the absence of obvious *IR* drops, suggesting a desirable reversibility and negligible internal resistance for the quasi-solid-state ZHSC. Especially, the voltage of the device can retain to 1.21 V (the initial voltage is 1.8 V) after 336 h (14 days) with a considerable low self-discharge rate of 1.75 mV h^{-1} (which is lower than the self-discharge rate of 2.02 mV h^{-1} in aqueous electrolyte, Fig. S15 in ESI†), confirming a remarkable electrochemical stability of the hydrogel/electrolyte to effectively prevent the occurrence of parasitic reactions (Fig. 7c).[24] The quasi-solid-state ZHSC also simultaneously delivers high gravimetric or areal energy densities and power densities (54.9 W h kg^{-1} at 75.8 W kg^{-1} and 111.9 μW h cm^{-2} at 154.5 μW cm^{-2}) as shown in Fig. 7d. The resulting energy densities outperform some of the reported quasi-solid-state energy storage systems, such as MXene-$NiCo_2S_4$@NF//AC@NF (27.24 W h kg^{-1} at 0.48 kW kg^{-1}), [88] AC//PVA//MXene (5.5 W h kg^{-1} at 500 W kg^{-1}), [89] 3D-graphene/graphite-paper based symmetric SC (8.8 W h kg^{-1} at 178.5 W kg^{-1} and 1.24 μW h cm^{-2} at 24.5 μW cm^{-2}),[90] WC-6ZnN-12U@CC//PAM//Zn@CC ZHS (27.7 W h kg^{-1} at 35.7 W kg^{-1}), [91] MXene/MPFs-6:1 based SC (20.4 μW h cm^{-2} at 152.2 μW cm^{-2}), [92] $Ti_3C_2T_x$ and Co-Al-LDH based asymmetric MHDs (8.84 μW h cm^{-2} at 0.23 mW cm^{-2}), [93] ASSS with 1T-MoS_2/Ti_3C_2 MXene (17.4 μW h cm^{-2} at 600 μW cm^{-2}), [94] MSC with MXene-rGO composite aerogel (2.18 μW h cm^{-2} at 60 μW cm^{-2}). [95]

Taking the soft configuration (graphite paper collector and PAM-co-PAA/κ-CG/$ZnSO_4$ hydrogel/electrolyte) discussed above into consideration, it is proposed that the assembled quasi-solid-state ZHSC could exhibit excellent flexibility to sustain external deformations. As shown in Fig. 7e, the cycling performance at 3 A g^{-1} of ZHSC is tested at different bending angles from 0 to 180°, and the corresponding specific capacities before and under bending deformations reveal small capacity difference with approximate 100% Coulombic efficiency, indicating the excellent anti-deformation stability of the quasi-solid-state ZHSC that perhaps results from the strong interactions between NMXC and hydrogel/electrolyte as well as the robust mechanical properties of PAM-co-PAA/κ-CG/$ZnSO_4$. Another interesting phenomenon comes from the excellent electrochemical stability of the quasi-solid-state ZHSC. As shown in Fig. 7f, 96.4% capacity retention for ZHSC can be maintained after 10000 cycles with about 100% Coulombic efficiency, which possibly originates from the enhancement of the electrochemical stability of the NMXC cathode couple by the satisfactory physiochemical confinement effects of the PAM-co-PAA/κ-CG polymer matrix for aqueous $ZnSO_4$ electrolyte without undesired leak problem. According to the corresponding GCD curves in the inset of Fig. 7f, similar curve shape can be observed for the initial 5 cycles and the last 5 cycles, further revealing a satisfactory electrochemical stability of the quasi-solid-state ZHSC. Moreover, the single device or series unit can directly power a light emitting diode (LED), calculagraph (normal working for 4 hours), or even a mobile phone, further demonstrating its promising potential for real applications (Fig. 7g-i).

3. Conclusions

In summary, a crumpled NMXC hybrid with N-doped MXene and N-doped carbon layer was successfully synthesized via a template-guided method. The characterization results manifest that the obtained heterogeneous sample possesses open interpenetrated frameworks with amorphous carbon protective layer and N-doping effect. The synergistic effect effectively exposes more electroactive sites, prevents the stacking of MXene flakes, and facilitates electrolyte ions transfer during charge storage process. The electrochemical test results demonstrate that NMXC exhibits a wider operating voltage window compared with pure MXene and better charge storage ability than NC. The DFT calculations further reveal a higher electronic conductivity of N-doped MXene and enhanced electrochemical oxidation resistance under higher positive potentials by N-doped carbon wrapping. Additionally, a dual crosslinked hybrid polymeric hydrogel/electrolyte of PAM-co-PAA/κ-CG/$ZnSO_4$ was also designed in this work. The test results

show that the κ-CG reinforces the mechanical properties and ionic conductivity. In addition, the quasi-solid-state ZHSC based on NMXC cathode and PAM-co-PAA/κ-CG/$ZnSO_4$ hydrogel/electrolyte demonstrates a high capacity with 96.4% capacity retention after 10000 cycles along with high energy/power densities of 54.9 W h kg^{-1} at 75.8 W kg^{-1}.

Conflicts of interest

There are no conflicts to declare.

Acknowledgements

The work was supported by the National Natural Science Foundation of China (Grant No. 21805237, 21965033, U2003216, U2003132), Natural Science Foundation of Xinjiang Uygur Autonomous Region (2018D01C053, 2019D01C075), Tianshan Youth Planning Program of Science&Technology Department of Xinjiang Uygur Autonomous Region (2018Q013), Scientific Research Program of the Higher Education Institution of Xinjiang (XJEDU2019I003), Tianchi Doctor Program of Education Department of Xinjiang Uygur Autonomous Region, Opening Foundation of the State Key Laboratory of Fine Chemicals (KF2003), "Talents Project" Key Training Object Project of Urumqi, and Doctor Starting Fund of Xinjiang University. The authors would like to thank Shiyanjia Lab (www.shiyanjia.com) for the measurement and analysis.

Notes and references

1 S. Hérou, J. J Bailey, M. Kok, P. Schlee, R. Jervis, D. J. L. Brett, P. R. Shearing, M. C. Ribadeneyra and M. Titirici, *Adv. Sci.*, 2021, **8**, 2100016.
2 M. Jakob and J. Hilaire, *Nature*, 2014, **517**, 150-151.
3 Y. Liang, H. Dong, D. Aurbach and Y. Yao, *Nat. Energy*, 2020, **5**, 646-656.
4 K. Leng, G. Li, J. Guo, X. Zhang, A. Wang, X. Liu, and J. Luo, *Adv. Funct. Mater.*, 2020, **30**, 2001317.
5 H. Zhang, Q. Liu, Y. Fang, C. Teng, X. Liu, P. Fang, Y. Tong and X. Lu, *Adv. Mater.*, 2019, **31**, 1904948.
6 Q. Wang, S. Wang, X. Guo, L. Ruan, N. Wei, Y. Ma, J. Li, M. Wang, W. Li and W. Zeng, *Adv. Electron. Mater.*, 2019, **5**, 1900537.
7 Y. Tian, Y. An, C. Wei, B. Xi, S. Xiong, J. Feng and Y. Qian, *ACS Nano*, 2019, **13**, 11676-11685.
8 X. Ma, J. Cheng, L. Dong, W. Liu, J. Mou, L. Zhao, J. Wang, D. Ren, J. Wu, C. Xu and F. Kang, *Energy Stor. Mater.*, 2019, **20**, 335-342.
9 T. Wang, Q. Zhang, J. Zhong, M. Chen, H. Deng, J. Cao, L. Wang, L. Peng, J. Zhu, and B. Lu. *Adv. Energy Mater.*, 2021, **11**, 2100448
10 X. Li, M. Chen, L. Wang, H. Xu, J. Zhong, M. Zhang, Y. Wang, Q. Zhang, L. Mei, T. Wang, J. Zhu, B. Lu, and X. Duan. *Nanoscale Horiz.*, 2020, **5**, 1586-1595.
11 T. Wang, H. Yang, and B. Lu. *J. Power Sources*, 2018, **399**, 105-114.
12 H. Luo, M. Chen, J. Cao, M. Zhang, S. Tan, L. Wang, J. Zhong, H. Deng, J. Zhu, and B. Lu. *Nano-Micro Lett.*, 2020, **12**, 113.
13 L. Wang, T. Wang, L. Peng, Y. Wang, M. Zhang, J. Zhou, M. Chen, J. Cao, H. Fei, X. Duan, J. Zhu, and X. Duan. *Natl. Sci. Rev.*, 2021, DOI: 10.1093/nsr/nwab050.
14 B. Wang, J. Li, C. Hou, Q. Zhang, Y. Li and H. Wang, *ACS Appl. Mater. Interfaces*, 2020, **12**, 46005-46014.
15 H. Wang, W. Ye, Y. Yang, Y. Zhong and Y. Hu, *Nano Energy*, 2021, **85**, 105942.
16 C. Wang, X. Zeng, P. J. Cullen and Z. Pei, *J. Mater. Chem. A*, 2021, **9**, 19054-19082.
17 Y. Shao, F. Shen and Y. Shao, *ChemElectroChem*, 2020, **8**, 484-491.
18 K. Wu, J. Huang, J. Yi, X. Liu, Y. Liu, Y. Wang, J. Zhang and Y. Xia, *Adv. Energy Mater.*, 2020, **10**, 1903977.
19 F. Wang, O. Borodin, T. Gao, X. Fan, W. Sun, F. Han, A. Faraone, J. A Dura, K. Xu and C. Wang, *Nat. Mater.*, 2018, **17**, 543-549.
20 T. Zhang, Y. Tang, S. Guo, X. Cao, A. Pan, G. Fang, J. Zhou and S. Liang, *Energy Environ. Sci.*, 2020, **13**, 4625-4665.
21 K. Li, X. Wang, S. Li, P. Urbankowski, J. Li, Y. Xu and Y. Gogotsi, *Small*, 2020, **16**, 1906851.
22 J. Nan, X. Guo, J. Xiao, X. Li, W. Chen, W. Wu, H. Liu, Y. Wang, M. Wu and G. Wang, *Small*, 2021, **17**, 1902085.
23 P. A. Maughan, N. Tapia-Ruiz and N. Bimbo, *Electrochim. Acta*, 2020, **341**, 136061.
24 Q. Yang, Z. Huang, X. Li, Z. Liu, H. Li, G. Liang, D. Wang, Q. Huang, S. Zhang, S. Chen and C. Zhi, *ACS Nano*, 2019, **13**, 8275-8283.
25 P. Zhang, R. A. Soomro, Z. Guan, N. Sun and B. Xu, *Energy Stor. Mater.*, 2020, **29**, 163-171.
26 M. Lu, W. Han, H. Li, H. Li, B. Zhang, W. Zhang and W. Zheng, *Adv. Mater. Interfaces*, 2019, **6**, 1900160.
27 H. Dong, J. Li, J. Guo, F. Lai, F. Zhao, Y. Jiao, D. J. L. Brett, T. Liu, G. He and I. P. Parkin, *Adv. Mater.*, 2021, **33**, 2007548.
28 X. Gong, Q. Yang, C. Zhi and P. S. Lee, *Adv. Energy Mater.*, 2020, **11**, 2003308.
29 Ø. Arlov, D. Rütsche, M. A. Korayem, E. Öztürk and M. Zenobi-Wong, *Adv. Funct. Mater.*, 2021, **31**, 2010732.
30 L. Yu, Z. Fan, Y. Shao, Z. Tian, J. Sun and Z. Liu, *Adv. Energy Mater.*, 2019, **9**, 1901839.
31 M. Alhabeb, K. Maleski, B. Anasori, P. Lelyukh, L. Clark, S. Sin and Y. Gogotsi, *Chem. Mater.*, 2017, **29**, 7633-7644.
32 C. Lei, C. Ji, H. Mi, C. Yang, Q. Zhang, S. He, Z. Bai and J. Qiu, *ACS Appl. Mater. Interfaces*, 2020, **12**, 53164-53173.
33 Y. Wen, T. E. Rufford, X. Chen, N. Li, M. Lyu, L. Dai and L. Wang, *Nano Energy*, 2017, **38**, 368-376.
34 A. Levitt, D. Hegh, P. Phillips, S. Uzun, M. Anayee, J. M. Razal, Y. Gogotsi and G. Dion, *Mater. Today*, 2020, **34**, 17-29.
35 Z. Wang, X. Li, C. Xuan, J. Li, Y. Jiang and J. Xiao, *Int. J. Energy Res.*, 2020, **45**, 2728-2738.
36 J. Wang, Z. Zhang, X. Yan, S. Zhang, Z. Wu, Z. Zhuang and W. Q. Han, *Nano-Micro Lett*., 2019, **12**, 4.
37 K. Qian, Q. Zhou, H. Wu, J. Fang, M. Miao, Y. Yang, S. Cao, L. Shi and X. Feng, *Compos. Part A: Appl. Sci. Manuf.*, 2021, **141**, 106229.
38 M. Q. Zhao, X. Xie, C. E. Ren, T. Makaryan, B. Anasori, G. Wang and Y. Gogotsi, *Adv. Mater.*, 2017, **29**, 1702410.
39 X. Li, X. Yin, C. Song, M. Han, H. Xu, W. Duan, L. Cheng and L. Zhang, *Adv. Funct. Mater.*, 2018, **28**, 1803938.

40 W. Bao, L. Liu, C. Wang, S. Choi, D. Wang and G. Wang, *Adv. Energy Mater.*, 2018, **8**, 1702485.
41 M. Han, J. Yang, J. Jiang, R. Jing, S. Ren and C. Yan, *J. Colloid Interface Sci.*, 2021, **582**, 1099-1106.
42 K. Zhao, X. Ma, S. Lin, Z. Xu and L. Li, *Chemistry Select*, 2020, **5**, 1890-1895.
43 Z. Pan and X. Ji, *J. Power Sources*, 2019, **439**, 227068.
44 T. Chen, G. Tong, E. Xu, H. Li, P. Li, Z. Zhu, J. Tang, Y. Qi and Y. Jiang, *J. Mater. Chem. A*, 2019, **7**, 20597-20603.
45 J. Chen, X. Yuan, F. Lyu, Q. Zhong, H. Hu, Q. Pan and Q. Zhang, *J. Mater. Chem. A*, 2019, **7**, 1281-1286.
46 R. Han and P. Wu, *J. Mater. Chem. A*, 2019, **7**, 6475–6481.
47 Z. Fan, C. Wei, L. Yu, Z. Xia, J. Cai, Z. Tian, G. Zou, S. X. Dou and J. Sun, *ACS Nano*, 2020, **14**, 867-876.
48 Y. Wan, K. Rajavel, X. Li, X. Wang, S. Liao, Z. Lin, P. Zhu, R. Sun and C.-P. Wong, *Chem. Eng. J.*, 2021, **408**, 127303.
49 D. Zuo, S. Song, C. An, L. Tang, Z. He and J Zheng, *Nano Energy*, 2019, **62**, 401-409.
50 L. Karlsson, J. Birch, J. Halim, M. Barsoum and P. O. Persson, *Nano lett.*, 2015, **15**, 4955-4960.
51 C. Du, Q. Liang, Y. Zheng, Y. Luo, H. Mao and Q. Yan, *ACS Appl. Mater. Interfaces*, 2018, **10**, 33779-33784.
52 Z. Wang, Z. Xu, H. Huang, X. Chu, Y. Xie, D. Xiong, C. Yan, H. Zhao, H. Zhang and W. Yang, *ACS Nano*, 2020, **14**, 4916-4924.
53 S. Zhao, H. Zhang, J. Luo, Q. Wang, B. Xu, S. Hong and Z. Yu, *ACS Nano*, 2018, **12**, 11193-11202.
54 J. Liu, H. Zhang, X. Xie, R. Yang, Z. Liu, Y. Liu and Z. Yu, *Small*, 2018, **14**, 1802479.
55 Y. Li, S. Yang, Z. Liang, Y. Xue, H. Cui and J. Tian, *Mater. Chem. Front.*, 2019, **3**, 2673-2680.
56 Z. Fan, Y. Wang, Z. Xie, X. Xu, Y. Yuan, Z. Cheng and Y. Liu, *Nanoscale*, 2018, **10**, 9642-9652.
57 J. Liu, H. B. Zhang, R. Sun, Y. Liu, Z. Liu, A. Zhou and Z. Z. Yu, *Adv. Mater.*, 2017, **29**, 1702367.
58 R. Zhao, H. Di, X. Hui, D. Zhao, R. Wang, C. Wang and L. Yin, *Energy Environ. Sci.*, 2020, **13**, 246-257.
59 L. Dong, W. Yang, W. Yang, C. Wang, Y. Li, C. Xu, S. Wan, F. He, F. Kang and G. Wang, *Nano-Micro Lett.*, 2019, **11**, 94.
60 M. Chen, J. Chen, W. Zhou, J. Xu and C.-P. Wong, *J. Mater. Chem. A*, 2019, **7**, 26524-26532.
61 S. Li, C. Yu, Y. Yang, X. Song, S. Chen, L. Song, B. Qiu, J. Yang, H. Huang, W. Guo, C. Zhao, M. Zhang, and J. Qiu, *Small*, 2018, **14**, 1803811.
62 S. He, F. Guo, Q. Yang, H. Mi, J. Li, N. Yang and J. Qiu, *Small*, 2021, **17**, 2100353.
63 Q. Wang, Y. Luo, R. Hou, S. Zaman, K. Qi, H. Liu, H. S. Park and B. Y. Xia, *Adv. Mater.*, 2019, **31**, 1905744.
64 S. Zeng, X. Shi, D. Zheng, C. Yao, F. Wang, W. Xu and X. Lu, *Mater. Res. Bull.*, 2021, **135**, 111134.
65 Z. Pan, F. Cao, X. Hua and X. Ji, *J. Mater. Chem. A*, 2019, **7**, 8984-8992.
66 J. Zhi, W. Zhao, X. Liu, A. Chen, Z. Liu and F. Huang, *Adv. Funct. Mater.*, 2014, **24**, 2013-2019.
67 Y. Luo, C. Yang, Y. Tian, Y. Tang, X. Yin and W. Que, *J. Power Sources*, 2020, **450**, 227694.
68 J. Fu, J. M. Yun, S. Wu, L. Li, L. Yu and K.-H. Kim, *ACS Appl. Mater. Interfaces*, 2018, **10**, 34212-34221.
69 F. Ran, T. Wang, S. Chen, Y. Liu and L. Shao, *Appl. Surf. Sci.*, 2020, **511**, 145627.
70 Z. Wang, X. Wang, Y. Bai, H. Yang, Y. Li, S. Guo, G. Chen, Y. Li, H. Xu and C. Wu, *ACS Appl. Mater. Interfaces*, 2019, **12**, 2481-2489.
71 J. Huang, S. Peng, J. Gu, G. Chen, J. Gao, J. Zhang, L. Hou, X. Yang, X. Jiang and L. Guan, *Mater. Horizons*, 2020, **7**, 2085-2096.
72 S. Liu and L. Li, *ACS Appl. Mater. Interfaces*, 2017, **9**, 26429-26437.
73 G. Geyik and N. Işıklan, *Int. J. Biol. Macromol.*, 2020, **152**, 359-370.
74 Y. Deng, M. Huang, D. Sun, Y. Hou, Y. Li, T. Dong, X. Wang, L. Zhang and W. Yang, *ACS Appl. Mater. Interfaces*, 2018, **10**, 37544-37554.
75 L. Ma, S. Chen, D. Wang, Q. Yang, F. Mo, G. Liang, N. Li, H. Zhang, J. A. Zapien and C. Zhi, *Adv. Energy Mater.*, 2019, **9**, 1803046.
76 X. Jiang, N. Xiang, J. Wang, Y. Zhao and L. Hou, *Carbohydr. Polym.*, 2017, **173**, 701-706.
77 J.-Y. Sun, X. Zhao, W. R. K. Illeperuma1, O. Chaudhuri, K. H. Oh, D. J. Mooney, J. J. Vlassak and Z. Suo, *Nature*, 2012, **489**, 133-136.
78 L. Han, H. Huang, X. Fu, J. Li, Z. Yang, X. Liu, L. Pan and M. Xu, *Chem. Eng. J.*, 2020, **392**, 123733.
79 S. Tarashi, H. Nazockdast and G. Sodeifian, *Polymer*, 2019, **183**, 121837.
80 Y. Huang, J. Liu, J. Zhang, S. Jin, Y. Jiang, S. Zhang, Z. Li, C. Zhi, G. Du and H. Zhou, *RSC Adv.*, 2019, **9**, 16313-16319.
81 L. Fan, L. Wang, S. Gao, P. Wu, M. Li, W. Xie, S. Liu and W. Wang, *Carbohydr. Polym.*, 2011, **86**, 1167-1174.
82 F. Mo, G. Liang, Q. Meng, Z. Liu, H. Li, J. Fan and C. Zhi, *Energy Environ. Sci.*, 2019, **12**, 706-715.
83 Z. Li, D. Chen, Y. An, C. Chen, L. Wu, Z. Chen, Y. Sun and X. Zhang, *Energy Stor. Mater.*, 2020, **28**, 307-314.
84 L. Zhou, X. Pei, K. Fang, R. Zhang and J. Fu, *Polymer*, 2020, **192**, 122319.
85 S. Liu and L. Li, *ACS Appl. Mater. Interfaces*, 2016, **8**, 29749-29758.
86 F. Mo, Z. Chen, G. Liang, D. Wang, Y. Zhao, H. Li, B. Dong and C. Zhi, *Adv. Energy Mater.*, 2020, **10**, 2000035.
87 S. Wu, Y. Chen, T. Jiao, J. Zhou, J. Cheng, B. Liu, S. Yang, K. Zhang and W. Zhang, *Adv. Energy Mater.*, 2019, **9**, 1902915.
88 H. Li, X. Chen, E. Zalezhad, K.N. Hui, K.S. Hui and M. J. Ko, *J. Ind. Eng. Chem.*, 2020, **82**, 309-316.
89 T.-H. Chang, T. Zhang, H. Yang, K. Li, Y. Tian, J. Y. Lee and P.-Y. Chen, *ACS Nano*, 2018, **12**, 8048-8059.
90 A. Ramadoss, K.-Y. Yoon, M.-J. Kwak, S.-I. Kim, S.-T. Ryu and J.-H. Jang, *J. Power Sources*, 2017, **337**, 159-165.
91 G. Lou, G. Pei, Y. Wu, Y. Lu, Y. Wu, X. Zhu, Y. Pang, Z. Shen, Q. Wu, S. Fu and H. Chen, *Chem. Eng. J.*, 2020, **413**, 127502.
92 W. Zhao, J. Peng, W. Wang, B. Jin, T. Chen, S. Liu, Q. Zhao and W. Huang, *Small*, 2019, **15**, 1901351.
93 S. Xu, Y. Dall'Agnese, G. Wei, C. Zhang, Y. Gogotsi and W. Han, *Nano Energy*, 2018, **50**, 479-488.
94 X. Wang, H. Li, H. Li, S. Lin, W. Ding, X. Zhu, Z. Sheng, H. Wang, X. Zhu and Y. Sun, *Adv. Funct. Mater.*, 2020, **30**, 0190302.
95 Y. Yue, N. Liu, Y. Ma, S. Wang, W. Liu, C. Luo, H. Zhang, F. Cheng, J. Rao, X. Hu, J. Su and Y. Gao, *ACS Nano*, 2018, **12**, 4224-4232.